Volume 7 | Number 16 | 21 August 2020

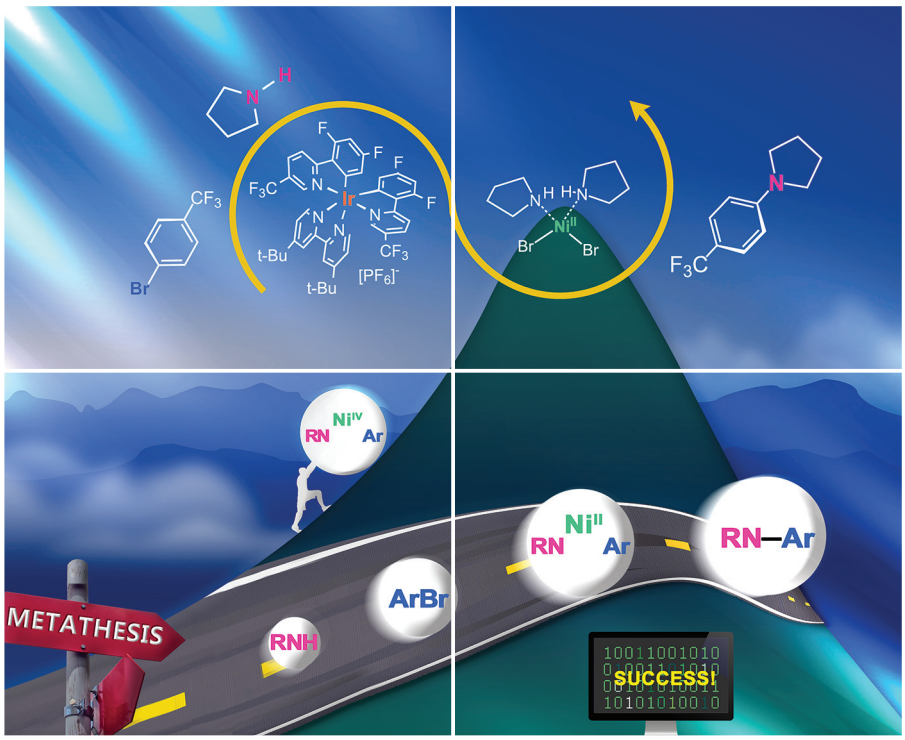

ORGANIC CHEMISTRY

FRONTIERS

CCS 中国化学会 CHINESE CHEMICAL SOCIETY
SIOC 1950
ROYAL SOCIETY OF CHEMISTRY
rsc.li/frontiers-organic

ORGANIC CHEMISTRY FRONTIERS

RESEARCH ARTICLE

View Article Online
View Journal | View Issue

Cite this: *Org. Chem. Front.*, 2020, **7**, 2168

Theoretical mechanistic study of metallaphotoredox catalysis: C–N cross-coupling *via* Ni(II)-mediated σ-bond metathesis†

Run-Han Li, [a] Bo Zhu, [a] Shuang Wang,[a] Yun Geng, [a] Li-Kai Yan, [a] Zhong-Min Su, [a] Li-Shuang Yao,[b] Rong-Lin Zhong *[c] and Wei Guan *[a,b]

The C–N cross-coupling reaction has been achieved by photoredox-mediated iridium/nickel dual catalysis, but its mechanism is still controversial in these reactions. A theoretical mechanistic study of the highly chemoselective C–N cross-coupling of pyrrolidine with 4-bromobenzotrifluoride has been performed using density functional theory (DFT) calculations. The oxidation state modulation mechanisms initiated by reductive quenching and oxidative quenching are unfavourable due to the mismatched redox potentials and slow electron transfer rates. In contrast, a radical mechanism merging reductive quenching (Ir^{III}–$*Ir^{III}$–Ir^{II}–Ir^{III}) and nickel catalytic cycles (Ni^{II}–Ni^{III}–Ni^{II}–Ni^{II}) is favourable. It consists of four major processes: exogenous base triggered successive single electron transfer (SET) and hydrogen atom transfer (HAT) to generate a nitrogen-centred radical, radical capture by nickel(II) dibromide, SET to regenerate iridium(III), and the rate-determining σ-bond metathesis to achieve the C–N cross-coupling. Furthermore, the suppression effect caused by α-substitution of pyrrolidine on the reaction is dominantly attributed to the steric effect rather than the electronic effect. Unlike the C–N cross-coupling, the concerted σ-bond metathesis involving nickel(II) is inapplicable for the C–O and C–S cross-couplings due to the high energy barriers. This study is expected to provide new mechanistic insights into metallaphotoredox-catalysed C–N cross-coupling.

Received 16th April 2020,
Accepted 1st July 2020

DOI: 10.1039/d0qo00458h

rsc.li/frontiers-organic

Introduction

Transition metal-catalysed cross-coupling reactions are currently important methods for constructing carbon–carbon (C–C) and carbon–heteroatom (C–X) bonds.[1] In particular, the formation of the C–N bond to access arylamines is of great significance, because these compounds widely exist in natural products, drugs, pharmaceuticals, organic materials and so on.[2] At present, copper has been widely utilized in C–N cross-coupling reactions because of its low cost, but it often requires high reaction temperatures and high catalyst loading.[3] In contrast, palladium, as the second most commonly used metal, can overcome the above disadvantages of copper due to its generality, practicality and relatively low catalyst loading.[4] However, the high cost of palladium is a major drawback. In this regard, it is quite necessary to develop a more economical and efficient C–N bond-based synthesis to avoid the problems in current coupling reactions. It is well known that photo-catalysed reactions have been widely applied in the area of synthetic organic chemistry because many reactions occur under mild conditions with the assistance of photocatalysts.[5] Recently, the formation of C–C and C–X bonds using iridium or ruthenium polypyridyl complexes[6] and organic dyes[7] as photoredox catalysts has been reported. Meanwhile, the intriguing synergy of photoredox-mediated bimetallic catalytic systems has also been widely investigated and rapidly attracted attention in the organic synthesis fields. Macmillan, Molander, Yoon and their co-workers have developed various cross-coupling reactions in these fields by the synergistic strategy of photocatalysts and transition metal catalysts.[8]

Iridium(III) polypyridyl complexes combining nickel(II) halides are the most widely used bimetallic synergistic cata-

[a]*Faculty of Chemistry, National & Local United Engineering Lab for Power Battery, Key Laboratory of Polyoxometalate Science of Ministry of Education, Northeast Normal University, Changchun 130024, People's Republic of China. E-mail: guanw580@nenu.edu.cn*
[b]*State Key Laboratory of Applied Optics, Changchun Institute of Optics, Fine Mechanics and Physics, Chinese Academy of Sciences, Changchun 130033, People's Republic of China*
[c]*Institute of Theoretical Chemistry, Jilin University, Changchun 130023, People's Republic of China. E-mail: zhongrl898@jlu.edu.cn*

†Electronic supplementary information (ESI) available: Computational details, Tables S1–S3, Scheme S1, Fig. S1–S10, and Cartesian coordinates of optimized structures in this work. See DOI: 10.1039/d0qo00458h

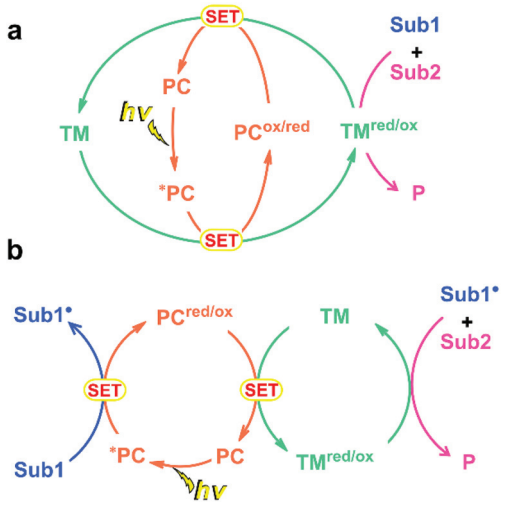

Scheme 1 Photoredox-mediated dual catalytic cycles: (a) oxidation state modulation mechanism. (b) Radical mechanism.

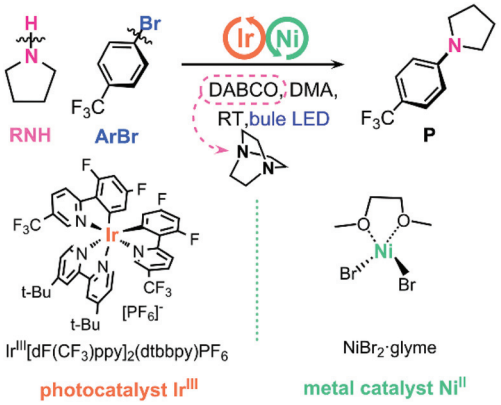

Scheme 2 Aryl amination by Ir^{III}/Ni^{II} metallaphotoredox catalysis.

lysts. In 2014, Molander and co-workers reported the organoboron cross-coupling of benzyltrifluoroborates with aryl bromides by Ir/Ni dual catalysis under mild conditions.[8a] They proposed a single-electron transfer (SET) mechanism, which is important to activate the organoboron reagents to a higher reactivity. In addition, Ir/Ni dual catalysis has been employed for a series of C–C cross-coupling reactions.[8b,9] Inspired by this strategy, MacMillan's group also developed the C–O cross-coupling reaction between alcohols and aryl bromides.[10] Besides, Johannes's group developed C–S and C–N cross-coupling reactions with Ir/Ni dual catalysis.[11] Recently, a series of metallaphotoredox-catalysed C–C and C–X couplings have been studied theoretically.[12] However, the mechanism of Ir/Ni dual catalysis is still intricate and unclear with regard to many mechanistic subtleties. In general, the proposed mechanisms of cross-coupling reactions involving photocatalysts can be divided into oxidation state modulation mechanism and radical mechanism (Scheme 1).[8c] In the oxidation state modulation mechanism, a photocatalyst (**PC**) would be excited by light to generate ***PC**, which can directly reduce or oxidise a transition metal catalyst (**TM**) to $\mathbf{TM}^{red/ox}$ through a SET process. The active $\mathbf{TM}^{red/ox}$ triggers the subsequent cross-coupling reactions of the substrates (**Sub1** and **Sub2**) (Scheme 1a). In the radical mechanism, the generated ***PC** would activate **Sub1** to form the corresponding radical ($\mathbf{Sub1}^{\bullet}$) and $\mathbf{PC}^{red/ox}$. Then $\mathbf{Sub1}^{\bullet}$ is trapped by $\mathbf{TM}^{red/ox}$, which is reduced or oxidised by $\mathbf{PC}^{red/ox}$ through a SET process, to deliver products (**P**) and complete the catalytic cycle (Scheme 1b). In our previous theoretical studies, the oxidation state modulation mechanism consisting of Ir^{III}–$*Ir^{III}$–Ir^{IV}–Ir^{III} oxidative quenching and Ni^{II}–Ni^{I}–Ni^{III}–Ni^{I}–Ni^{II} catalytic cycles is favourable for C–O and C–S cross-couplings.[12a,b] Recently, MacMillan *et al.* reported the photoredox-mediated Ir/Ni dual-catalysed aryl amination reaction of pyrrolidine with 4-bromobenzotrifluoride (Scheme 2).[13] They proposed a different oxidation state modulation mechanism involving the Ni(0) complex formed by the reduction of Ni(II) salt by a mild sacrificial reagent. However, there are many uncertainties about the species of reductive reagents due to the complexity of the actual reaction environment. According to Ma and co-workers' theoretical investigation,[14] the photocatalyst and 1,4-diazobicyclo[2.2.2] octane (DABCO) play important roles for generating the active nickel(0) species. The reaction mechanism involving Ni(0) active species reproduces the experimental proposal. However, the photoexcited *Ir(III) may be quenched by several species such as the transition metal catalyst Ni(II) complex, base DABCO, or even substrate pyrrolidine. The reaction mechanisms become very complicated when all of these quenching possibilities for *Ir(III) are considered. It is noteworthy that an appropriate amount of base is an indispensable condition in the reaction, which may accelerate hydrogen atom transfer (HAT) and participate in the formation process of amino radicals.[9a] The insertion of amino radicals to ground-state Ni(II) species is expected to afford Ni(III)-amide complexes, thereby enabling the favourable Ni(III) C–N reductive elimination. On the other hand, $Ni^{II}(bpy)Cl_2$ can completely quench photoexcited *Ir(III), which is confirmed by our previous emission quenching experiments.[12a] Hence, a comprehensive study with the consideration of *Ir(III) quenching mechanisms, role of DABCO, amino radical formation and subsequent C–N cross-coupling is worthwhile.

In the present work, we aim to reveal the mechanism of the C–N cross-coupling reaction, to clarify the nickel catalytic cycles and to understand the role of the base. Meanwhile, we also want to explore the differences among the C–N with the C–O and C–S cross-coupling reactions by Ir/Ni dual catalysis. A radical mechanism consisting of Ir-mediated reductive quenching, DABCO-mediated HAT and nickel-mediated C–N bond formation is the most favourable pathway for C–N cross-coupling, which is different from the C–O and C–S cross-couplings. These findings provide new perspectives for constructing the C–N bond and a comprehensive understanding of C–N cross-coupling reactions by photoredox-mediated dual catalysis.

Computational models and details

Computational methods

All of the calculations were performed with the (U)M06 functional,[15] referring to the benchmark calculations in our previous studies.[12a,b,16] A pruned numerical integration grid (99 590) was used *via* the keyword Int = Ultrafine. The 6-31++G (d,p) basis set was used for H atom involved in the HAT process. The LanL2DZ basis sets[17] were used for the Ni, Ir atoms, while 6-31G(d) basis sets were employed for other main-group atoms. Frequencies were calculated at the same theoretical level to verify the stationary points to be equilibria or transition states. Intrinsic reaction coordinate (IRC) calculations were carried out to ensure the correct transition states connecting reactants and products.[18] A better basis set system was employed to evaluate the single-point energy, and combined it with the gas phase Gibbs free energy corrected by the thermodynamic energy[19] to assess the free energy at 298.15 K and 1 atm in this work. The SMD solvent model[20] with the parameters for *N*,*N*-dimethylacetamide (DMA) was used for the solution phase single-point energy calculations with the SDD basis sets[21] for Ni, Ir atoms and 6-311++G(d, p) basis sets for others. All of the above calculations were performed with Gaussian 09 program.[22] The 3D molecular structures were printed using CYLview program.[23]

In order to describe the SET processes, the corresponding Gibbs activation energy ($\Delta G^{\circ\ddagger}$) and the electron transfer rate constant (k) were obtained based on Marcus–Hush theory,[24] which can be expressed as:

$$\Delta G^{\circ\ddagger} = \frac{(\Delta G + \lambda)^2}{4\lambda} \quad (1)$$

$$k = \sqrt{\frac{4\pi^3}{h^2 \lambda k_B T}} |V_{DA}|^2 \exp\left(-\frac{(\Delta G + \lambda)^2}{4\lambda k_B T}\right) \quad (2)$$

where λ is the reorganization energy, ΔG is the Gibbs free energy change for the electron transfer reaction, k_B is the Boltzmann constant, h is Planck's constant, V_{DA} is the electronic coupling (charge-transfer integral) between the donor and acceptor, and T is the temperature (T = 298.15 K in the present calculations); see the ESI for details.†

Model reaction

As shown in Scheme 2, the C–N cross-coupling of aryl bromide and pyrrolidine by Ir^{III}/Ni^{II} metallaphotoredox catalysis was selected as the model reaction.[13] In the present calculations, we adopted pyrrolidine (**RNH**) and 4-bromobenzotrifluoride (**ArBr**) as substrates, $NiBr_2$·glyme as the transition metal catalyst, DABCO as the exogenous base, and $Ir^{III}[dF(CF_3)ppy]_2(dtbbpy)PF_6$ (**Ir(III)**) as the photocatalyst, respectively. The absorption spectra of photocatalyst **Ir(III)** were simulated at the SMD(acetonitrile)/(U)M06/[6-31G(d)/LanL2DZ(Ir)] level (see Fig. S1, S2 and Table S1†). The experimental redox potentials of iridium complexes were well reproduced by the present calculations (Table S2†). In addition, the $Ni(RNH)_2Br_2$ complex (**RNH** as the ligand) was regarded as the active species of the transition metal catalytic cycle[14] and the triplet $Ni(RNH)_2Br_2$ ($\mathbf{Ni(II)^T}$) is more stable than the singlet ($\mathbf{Ni(II)^S}$) by 14.7 kcal mol^{-1} (Fig. S3†).

Results and discussion

Oxidation state modulation mechanism initiated by reductive quenching

Inspired by the experimentally proposed mechanism,[13] we first inspected a dual catalytic cycle merging Ir^{III}–$*Ir^{III}$–Ir^{II}–Ir^{III} and Ni^0–Ni^{II}–Ni^{III}–Ni^{I}–Ni^0, as shown in Fig. 1. The reaction is initiated by $Ni^0(RNH)_2(ArBr)$, where two **RNH** and one **ArBr** as ligands simultaneously coordinate with the nickel centre. The first elementary step is the oxidative addition of the C–Br bond of **ArBr** to the nickel(0) centre. The triplet and singlet surfaces cross in this step because there are similar structures of stationary points in both energy surfaces. The spin inversion alters the favourable reaction pathway through the minimum energy crossing point (MECP). Although the singlet $Ni^0(RNH)_2(ArBr)$ (denoted as $\mathbf{Ni(0)^S}$) lies lower than the triplet (denoted as $\mathbf{Ni(0)^T}$) by 13.4 kcal mol^{-1}, the subsequent singlet surface lies higher than the triplet surface (Fig. S4†). In the favourable pathway, the C–Br bond is cleaved *via* the singlet transition state **TSa1** and MECP to afford a triplet nickel(II) aryl bromide intermediate **a2** with a moderate $\Delta G^{\circ\ddagger}$ value of 10.8 kcal mol^{-1} and a Gibbs free energy change (ΔG°) of −30.2 kcal mol^{-1}. Then, the approach of DABCO toward **a2** generates a stable intermediate **a3** (ΔG° = −3.7 kcal mol^{-1}), where the H atom of the **RNH** ligand of **a2** binds with the N atom of DABCO through near linear N···H–N hydrogen-bonding interaction. Subsequently, a σ-bond metathesis between Ni–Br and H–N (**RNH**) bonds occurs *via* a four-centred (Ni–N–H–Br) transition state **TSa2** to afford a nickel(II) aryl amino intermediate **a4**. The $\Delta G^{\circ\ddagger}$ and ΔG° values of this step are 22.3 and 21.3 kcal mol^{-1}, respectively. The photoexcited ***Ir(III)** can then facilitate the oxidation of **a4** to deliver the nickel(III) aryl amino bromide intermediate **a5** and reduced **Ir(II)** species. This SET process is exoergic of 34.2 kcal mol^{-1}. The C–N reductive elimination occurs through the transition state **TSa3** to provide the target product **P** and a three-coordinate Ni(I) bromide intermediate **a6** with a moderate $\Delta G^{\circ\ddagger}$ value of 14.5 kcal mol^{-1} and a large negative ΔG° value of −32.4 kcal mol^{-1}. Finally, $\mathbf{Ni(0)^S}$ and **Ir(III)** are expected to be regenerated through the second SET process between **Ir(II)** and **a6**. Unlike the first SET, however, the second SET process is endergonic by 11.6 kcal mol^{-1}. Furthermore, the calculated redox potentials have also shown that **Ir(II)** ($E_{1/2}[Ir^{III}/Ir^{II}]$ = −1.50 V *vs.* SCE in DMA) is not able to reduce Ni(I) ($E_{1/2}[Ni^I/Ni^0]$ = −1.75 V *vs.* SCE in DMA) to form the Ni(0) complex. Thus, the endoergic demand of the second SET and the mismatched redox potentials may exclude such oxidation state modulation mechanism initiated by reductive quenching.

Oxidation state modulation mechanism initiated by oxidative quenching

Inspired by the theoretical mechanistic studies of iridium/nickel metallaphotoredox-catalysed C–O and C–S cross-coup-

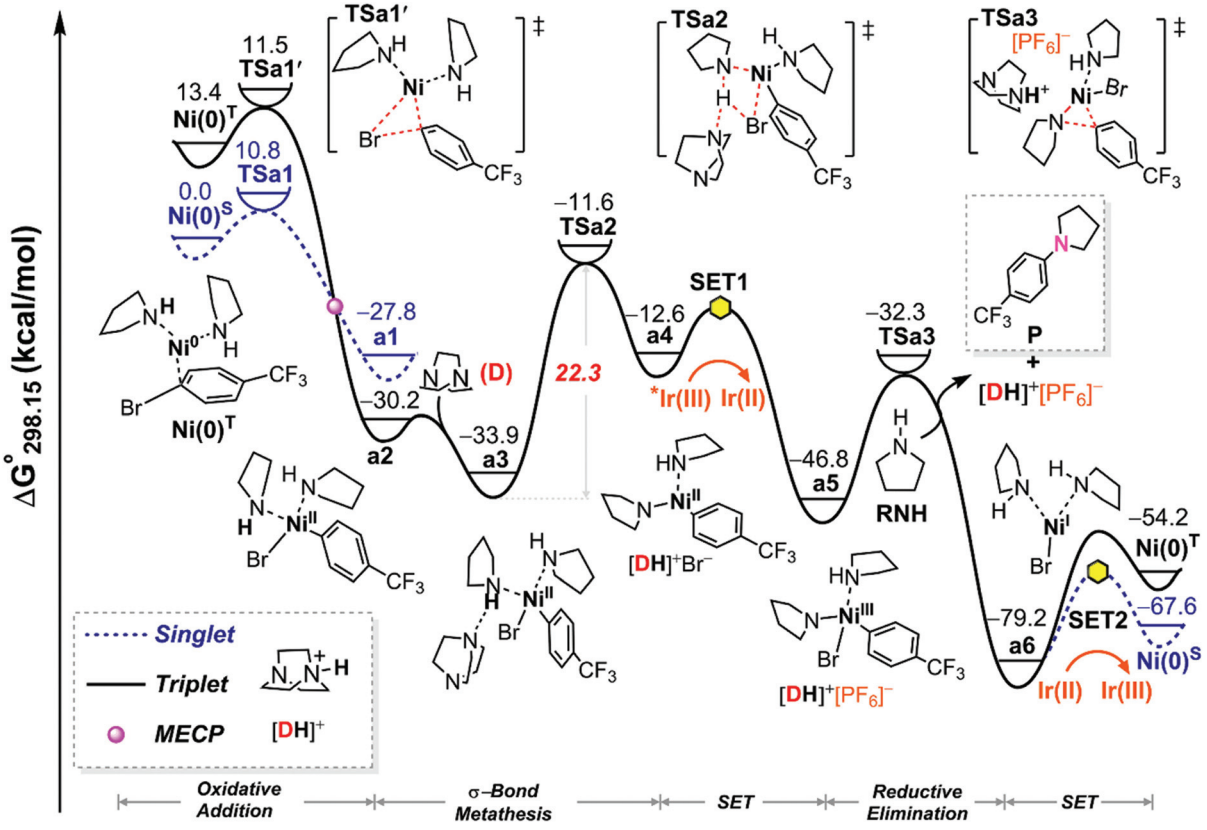

Fig. 1 Gibbs energy profiles ($\Delta G°_{298.15}$) of the oxidation state modulation mechanism merging Ir^{III}–$*Ir^{III}$–Ir^{II}–Ir^{III} reductive quenching and Ni^{0}–Ni^{II}–Ni^{III}–Ni^{I}–Ni^{0} catalytic cycles.

lings, wherein the catalytic cycles merging Ir^{III}–$*Ir^{III}$–Ir^{IV}–Ir^{III} and Ni^{II}–Ni^{I}–Ni^{III}–Ni^{I}–Ni^{II} were reported,[12] we further questioned whether such oxidation state modulation mechanism initiated by oxidative quenching is also applicable to the present C–N cross-coupling. As shown in Fig. 2, the photoexcited ***Ir(III)** is oxidatively quenched by **Ni(II)^{T}** *via* the SET process to afford the ground-state **Ir(IV)** and an active nickel(I) bromide species **b1**. This oxidative quenching step is exoergic of 7.2 kcal mol^{-1}. After hydrogen-bonding interaction of DABCO with **b1**, an oxidative addition of the C–Br bond of **ArBr** to the nickel(I) centre of **b2** occurs *via* the transition state **TSb1** to afford a nickel(III) aryl dibromide intermediate **b3**. The $\Delta G^{\circ\ddagger}$ and $\Delta G°$ of this step are 20.5 and −2.6 kcal mol^{-1}, respectively. In contrast, an alternative pathway involving the proton transfer from **b2** was also evaluated to require a much larger $\Delta G^{\circ\ddagger}$ value of 30.3 kcal mol^{-1} than the present one (Fig. S5†). Subsequently, the DABCO moiety of **b3** can abstract one H atom of the **RNH** moiety as a proton *via* the transition state **TSb2** to afford the nickel(III) intermediate **b4**. The DABCO-assisted proton transfer (DABCO-PT) step needs to overcome a small $\Delta G^{\circ\ddagger}$ value of 10.2 kcal mol^{-1} and a positive $\Delta G°$ value of 10.1 kcal mol^{-1}. Then, C–N reductive elimination followed by ligand exchange occurs through the transition state **TSb3** to form the nickel(I) intermediate **b5** and the desired product **P**. This reductive elimination from the nickel(III) complex requires a $\Delta G^{\circ\ddagger}$ value of 15.1 kcal mol^{-1} relative to **b3**. Finally, **b5** reacts with **Ir(IV)** through an exergonic SET process ($\Delta G°$ = −38.9 kcal mol^{-1}) to regenerate **Ni(II)^{T}** and **Ir(III)**. Thus, the above results show that the rate-determining step is oxidative addition with a $\Delta G^{\circ\ddagger}$ value of 20.5 kcal mol^{-1}, which indicates that the oxidation state modulation mechanism initiated by oxidative quenching is a competitive pathway for the present C–N cross-coupling.

Radical mechanism initiated by reductive quenching

Formation of the nitrogen-centred radical derived from pyrrolidine. In addition to the nickel(II) complexes, DABCO can reductively quench photoexcited ***Ir(III)** to deliver a radical ion-pair [DABCO$^{\bullet+}$][PF_6^-] (DABCO$^{\bullet+}$) and reduced **Ir(II)** species with a $\Delta G°$ value of −11.6 kcal mol^{-1}, as shown in Fig. 3. This SET step is also supported by the matched redox potentials ($E_{1/2}$[$*Ir^{III}/Ir^{II}$] = 1.05 V *vs.* SCE in DMA and $E_{1/2}$[DABCO$^{\bullet+}$/DABCO] = 0.53 V *vs.* SCE in DMA). Furthermore, the activation barrier of this SET step is only 3.2 kcal mol^{-1} based on the Marcus–Hush theory.[24] Subsequently, the nitrogen-centred radical coupling partner **RN$^{\bullet}$** is generated through a hydrogen atom transfer (HAT) from **RNH** to DABCO$^{\bullet+}$. The HAT process needs a very small activation barrier of 1.3 kcal mol^{-1}. In contrast, two other possibilities for the generation of α- and β-carbon-centred radicals by HAT were also evaluated to be less favourable than the present one (Fig. S6†).

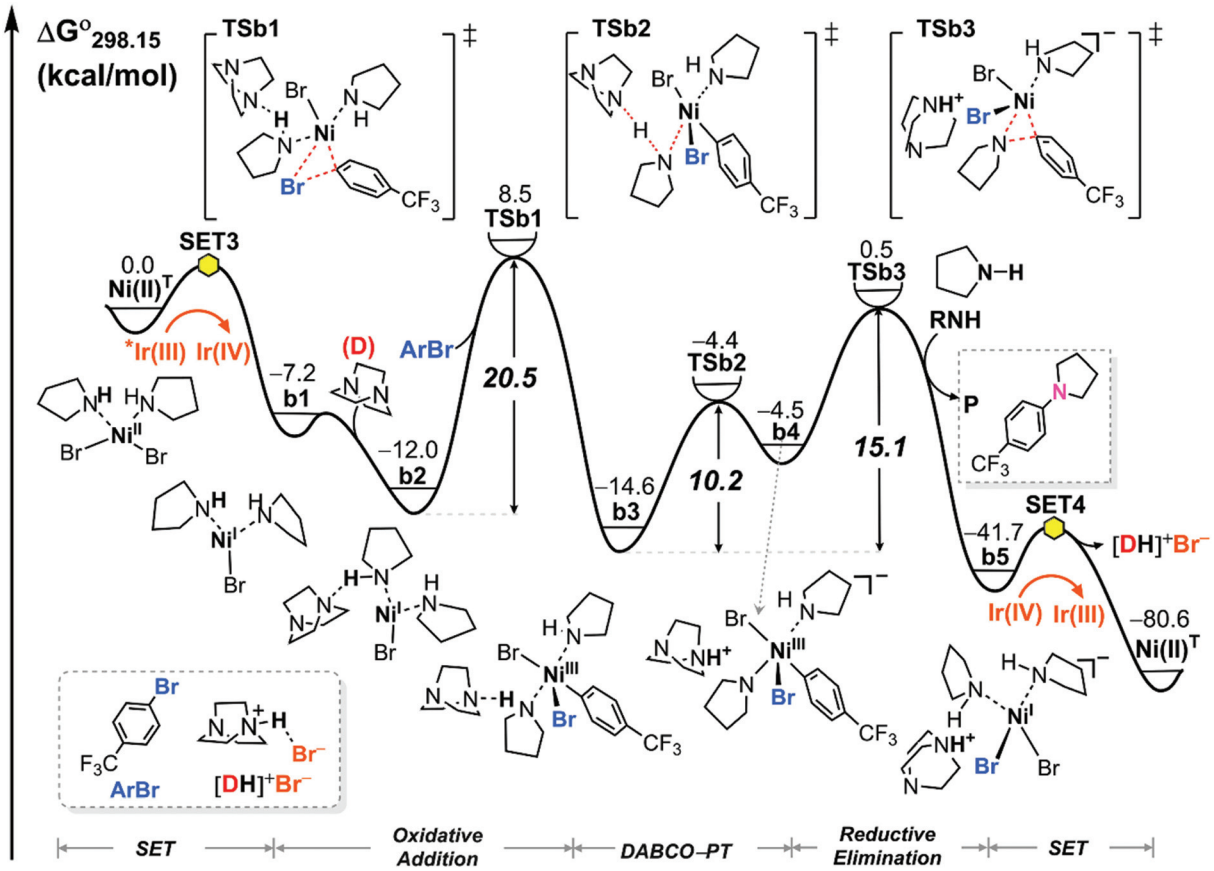

Fig. 2 Gibbs energy profile ($\Delta G°_{298.15}$) of the oxidation state modulation mechanism merging Ir^{III}–$*Ir^{III}$–Ir^{IV}–Ir^{III} oxidative quenching and Ni^{II}–Ni^{I}–Ni^{III}–Ni^{I}–Ni^{II} catalytic cycles.

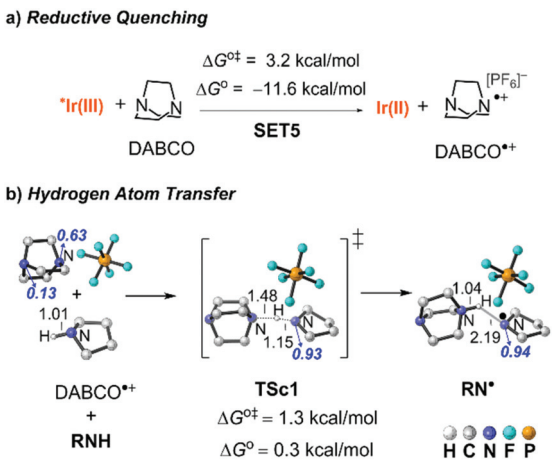

Fig. 3 (a) $\Delta G°^{‡}$ and $\Delta G°$ of reductive quenching of *Ir(III) triggered by DABCO; (b) $\Delta G°^{‡}$, $\Delta G°$, and optimized structures of the hydrogen atom transfer process (selected bond distances are given in angstroms with black non-italic font and spin densities are given in blue italic font).

C–N cross-coupling. The above SET-mediated catalysis converts **RNH** to the reactive radical **RN**$^{•}$ as a nucleophilic coupling partner that subsequently is involved in the nickel catalysed cycle. As depicted in Fig. 4, the active radical **RN**$^{•}$ is captured by **Ni(II)**^{T} to afford a nickel(III) amino dibromide intermediate **c1** and dissociate an ion pair $[DABCOH]^{+}[PF_6]^{-}$ (**A**) with a small $\Delta G°$ value of −1.0 kcal mol^{-1}. Then, the single electron reduction of **c1** by **Ir(II)** delivers a stable nickel(II) amino bromide intermediate **c2** and regenerates the photocatalyst **Ir(III)** with a large energy downhill of 31.6 kcal mol^{-1}. Note that the ground state for **c2** is the triplet state that lies below the singlet state by 16.3 kcal mol^{-1}. Starting from triplet **c2**, two possibilities have been investigated: one is the concerted σ-bond metathesis to achieve the C–N cross-coupling and the other is the stepwise oxidative addition and reductive elimination to form the target C–N bond. The former σ-bond metathesis pathway (**c2** → **TSc2** → **c3**) occurs more favourably than the latter (**c2** → **TSc3** → **c4** → **TSc4** → **c3**), and the activation barriers of these two pathways are 18.1 and 27.1 kcal mol^{-1}, respectively. In the **c2** → **TSc2** → **c3** transformation, a σ-bond metathesis between Ni–N and Br–C(Ar) bonds occurs *via* the transition state **TSc2** to yield a nickel(II) dibromide complex **c3**. In the four-membered-ring (Ni–N–C–Br) **TSc2**, the Ni–N and C–Br distances are elongated to 2.00 Å and 2.04 Å from 1.83 Å in **c2** and 1.90 Å in **ArBr**, whereas the Ni–Br and C–N distances are reduced to 2.65 Å and 2.14 Å, respectively. These geometrical changes indicate that the C–Br bond cleavage and the C–N bond formation occur simultaneously. In

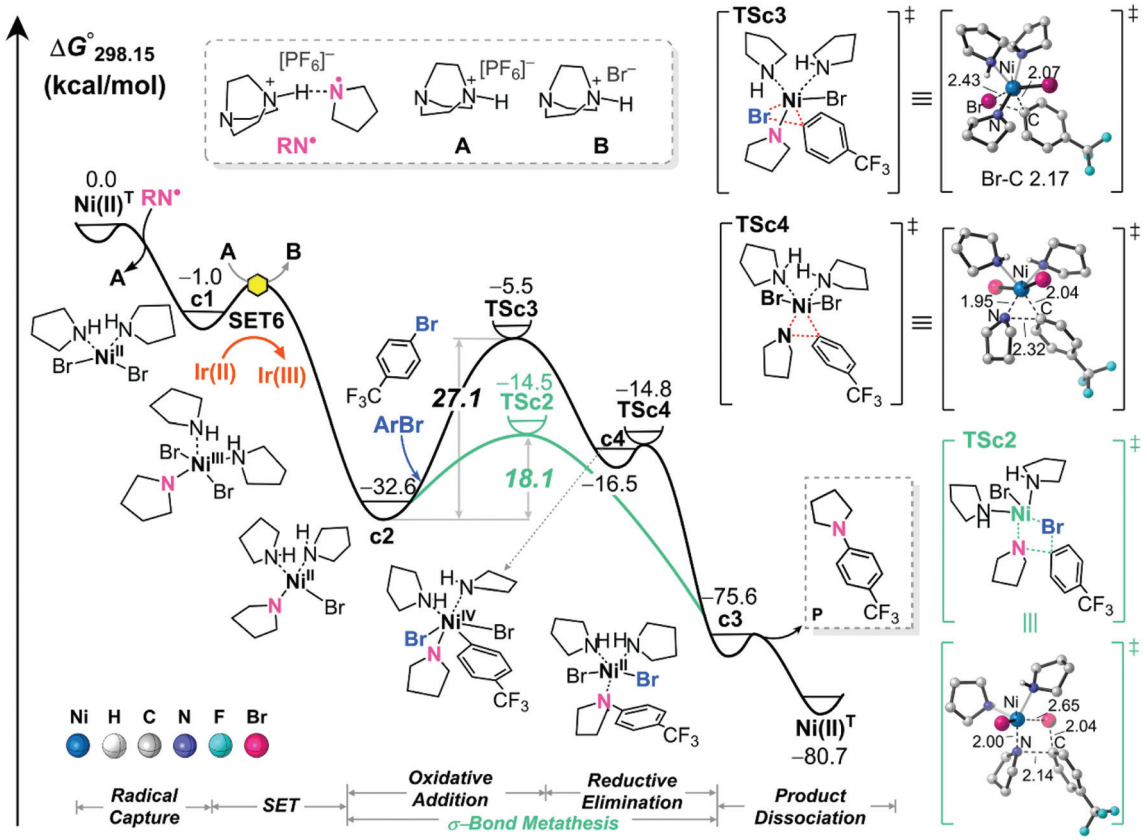

Fig. 4 Gibbs energy profiles ($\Delta G°_{298.15}$) of the radical mechanism merging Ir^{III}–$*Ir^{III}$–Ir^{II}–Ir^{III} reductive quenching and Ni^{II}–Ni^{III}–Ni^{II}–Ni^{II} catalytic cycles.

the **c2** → **TSc3** → **c4** → **TSc4** → **c3** transformation, the unfavourable oxidative addition of **ArBr** to the nickel(II) centre of **c2** occurs through the transition state **TSc3** to afford the unstable six-coordinate nickel(IV) intermediate **c4** with a large $\Delta G°^{‡}$ value of 27.1 kcal mol^{-1} and a positive $\Delta G°$ value of 16.1 kcal mol^{-1}, although the subsequent C–N reductive elimination requires a very small energy barrier of 1.7 kcal mol^{-1}. Finally, the desired aniline product is spontaneously dissociated from **c3** and the **Ni(II)^T** is regenerated. This product dissociation is exergonic by 5.1 kcal mol^{-1}.

Quenching mechanism of photoexcited *Ir(III)

Based on the discussion of the above three mechanisms, the oxidation state modulation mechanism initiated by oxidative quenching and the radical mechanism initiated by reductive quenching are competitive, but the latter is more favourable. The difference between these two mechanisms originates from the quenching mechanism of photoexcited ***Ir(III)**, one refers to SET3 in Fig. 2 ($*Ir^{III} + Ni^{II} \rightarrow Ir^{IV} + Ni^{I}$), the other refers to SET5 in Fig. 3 ($*Ir^{III}$ + DABCO → Ir^{II} + $DABCO^{•+}$). In order to better understand the ***Ir(III)** quenching mechanism, further kinetic exploration of SET3 and SET5 processes has been performed. To choose a reasonable model, one hundred donor–acceptor molecular clusters were sampled randomly using Molclus program,[25] and then optimized with the UFF force field.[26] Finally, the conformers with ≥5% probability in the Boltzmann distribution were screened out for optimization at the (U)M06/[6-31G(d)/LanL2DZ(Ni,Ir)] level (Fig. S7†). The selected most stable dimer configurations **Ir(III)/Ni(II)** and DABCO/**Ir(III)** were employed to further evaluate the electron transfer rate related parameters of SET3 and SET5 by Marcus–Hush theory, as listed in Table 1. The SET3 process involved in the oxidative quenching cycle occurs with an energy barrier of 0.20 eV and the electron transfer rate of 5.95×10^8 s^{-1}. In contrast, the SET5 process involved in the reductive quenching cycle occurs with an energy barrier of 0.14 eV and the electron transfer rate of 2.60×10^{10} s^{-1}. Therefore, the reductive quenching of photoexcited ***Ir(III)** to **Ir(II)** is faster by DABCO

Table 1 Kinetic calculation of the electron transfer rate related parameters for the SET3 and the SET5

	ΔG_r (eV)	$\Delta G°^{‡}$ (eV)	λ (eV)	V (eV)	k_{SET} (s^{-1})
SET3	−0.31	0.20	1.35	−0.01	5.95×10^8
SET5	−0.40	0.14	1.23	−0.02	2.60×10^{10}

λ_i, the inner reorganization energy; λ_o, the solvent reorganization energy; ΔG_r, the reaction energy; $\Delta G°^{‡}$, the Gibbs activation energy; $\lambda = \lambda_i + \lambda_o$; V, electron coupling value; k_{SET}, the electron transfer rate constant using the Marcus–Hush theory.

than **Ni(II)^{T}**, which is consistent with the previous experimental proposals and theoretical calculations.[14,27]

Tolerance of σ-bond metathesis

Substituent effect of pyrrolidine. It can be concluded from the above results that the radical mechanism merging Ir^{III}–$*Ir^{III}$–Ir^{II}–Ir^{III} reductive quenching and Ni^{II}–Ni^{III}–Ni^{II}–Ni^{II} catalytic cycles is favourable. The rate-determining step is the σ-bond metathesis with an energy barrier of 18.1 kcal mol^{-1}. According to the experimental results, α-substitution on the amine substrate provides a lower yield than unsubstituted **RNH** (*e.g.*, 2-methylpyrrolidine (**RNH–CH$_3$**) 60% yield *vs.* **RNH** 96% yield).[13] In order to further verify the rationality of the radical mechanism, the substituent effect of pyrrolidine on the σ-bond metathesis was evaluated. The four-centre σ-bond metathesis using **RNH–CH$_3$** as the substrate needs an energy barrier of 23.5 kcal mol^{-1}, which is larger than that using **RNH** by 5.4 kcal mol^{-1} (Fig. S8†). The reasons of this difference have been analysed from two perspectives, the electronic effect and steric effect. First, we investigated the electronic processes of σ-bond metathesis with frontier orbital and NBO population analyses.[28] Fig. 5a illustrates the highest occupied molecular orbitals (HOMOs) of some selected points on the intrinsic reaction coordinate (IRC) path of **c2** → **TSc2** → **c3**. The $3d_{Ni}$, $2p_{RN}$, π_{Ar} and $4p_{Br}$ orbitals are mainly involved in this transformation. As shown in Fig. 5b, the gradual elongation of Ni–N bond decreases the Ni atomic population (especially the Ni 3d orbital) but increases the atomic population of the N 2p orbital in the RN moiety. Subsequently, the gradually approaching between the RN and Ar moieties decreases the atomic population of RN but increases that of the Ar π orbital. Meanwhile, when Br moves away from Ar to Ni, the atomic population of the Ar moiety decreases, whereas that of Br moiety monotonically increases. The NBO population analysis reveals an annular charge transfer ($3d_{Ni} \rightarrow 2p_{RN} \rightarrow \pi_{Ar} \rightarrow 4p_{Br}$). Similar charge transfer characteristics can be found in the σ-bond metathesis of **c2-CH$_3$** → **TSc2-CH$_3$** → **c3-CH$_3$**, as shown in Fig. 5c and d. Thus, the electronic effect caused by the methyl substitution of α-hydrogen cannot be responsible for the energy barrier difference.

Subsequently, the steric effect was investigated. We calculated the buried volumes[29] (%V_{Bur}) of two different complexes **c2** and **c2-CH$_3$** within a radius of around 3.5 Å, which confirms the significant differences in steric hindrance, as shown in Fig. 6. First, we define the *z*-axis as perpendicular to the plane formed by nickel and the two pyrrolidine ligands. Meanwhile, **ArBr** moieties in the **c2** and **c2-CH$_3$** were removed in order to analyse the steric effect. The steric maps indicated that the Ni centre of **c2** (%V_{Bur} = 68.7) is less sterically congested than that of **c2-CH$_3$** (%V_{Bur} = 74.5). Similar results can be found from the buried volume calculation along the ligand direction with nickel as the centre (Fig. S9†). Furthermore, we also used the activation strain model[30] to analyse the effect of steric hindrance on the energy barrier of σ-bond metathesis (Fig. S10†). It can be suggested that the increased distortion energy of **c2** and **ArBr** moieties caused by methyl substitution plays a major role in the higher energy barrier. Therefore, such steric repulsion clearly suppresses the rate-determining σ-bond meta-

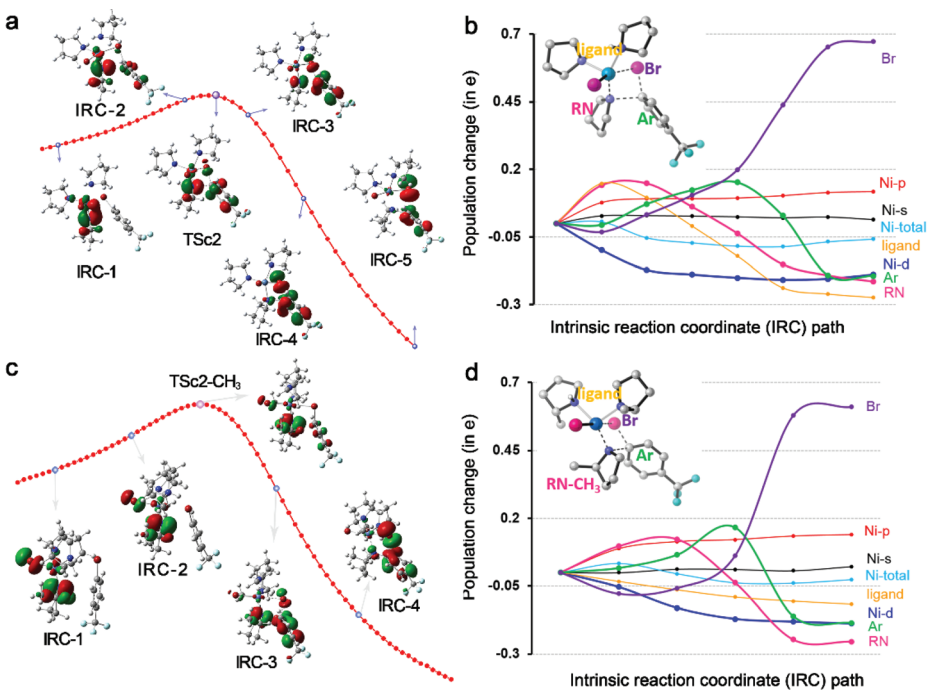

Fig. 5 (a) HOMOs of some selected points on the IRC path of c2 → TSc2 → c3. (b) Changes in atomic population (in e) on the IRC path of c2 → TSc2 → c3. (c) HOMOs of some selected points on the IRC path of c2-CH$_3$ → TSc2-CH$_3$ → c3-CH$_3$. (d) Changes in atomic population (in e) on the IRC path of c2-CH$_3$ → TSc2-CH$_3$ → c3-CH$_3$.

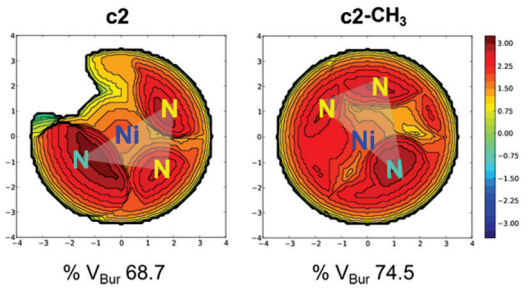

Fig. 6 Steric crowding maps perpendicular to the Ni–N–N plane together with the buried volume for **c2** and **c2-CH$_3$**.

thesis, thereby decreasing the reaction rate. These results reproduce well the experimental results that amines lacking α-hydrogens cannot provide a good reaction yield.[13]

Applicability of σ-bond metathesis to C–O and C–S cross-couplings. In order to examine the applicability of σ-bond metathesis involving nickel(II), comparisons between σ-bond metathesis and oxidative addition steps have been performed on the C–N, C–O and C–S cross-coupling reactions, where **ArBr** was employed as a constant substrate, and the second substrate was chosen from **RNH**, benzyl alcohol (**ROH**) and 4-methoxybenzyl thiol (**RSH**), respectively. As shown in Fig. 7, the concerted σ-bond metathesis is more favourable than the stepwise oxidative addition and reductive elimination to achieve the C–N, C–O and C–S cross-couplings. When the nitrogen-centred radical coupling partner **RN$^{\bullet}$** in the **c2** → **TSc2** → **c3** transformation is replaced with **RO$^{\bullet}$** and **RS$^{\bullet}$**, the energy barriers of σ-bond metathesis are significantly increased by 10.2 and 14.2 kcal mol^{-1}, respectively (Fig. 7a, c and d). This suggests that the σ-bond metathesis involving nickel(II) is inapplicable for the C–O and C–S cross-couplings. In fact, our previous calculations indicate that the oxidation state modulation mechanism consisting of Ir^{III}–*Ir^{III}–Ir^{IV}–Ir^{III} oxidative quenching and Ni^{II}–Ni^{I}–Ni^{III}–Ni^{I}–Ni^{II} catalytic cycles is favourable for C–O and C–S cross-couplings.[12]

In addition, when two **RNH** in the **c2** → **TSc2** → **c3** transformation are replaced with the 2,2′-bipyridyl (bpy) ligand, the energy barrier of σ-bond metathesis is slightly increased by 1.7 kcal mol^{-1} (Fig. 7a and b). This result can help us understand why the aryl amination using ligand-free nickel(II) salts and photoredox catalysis is advantageous.[13]

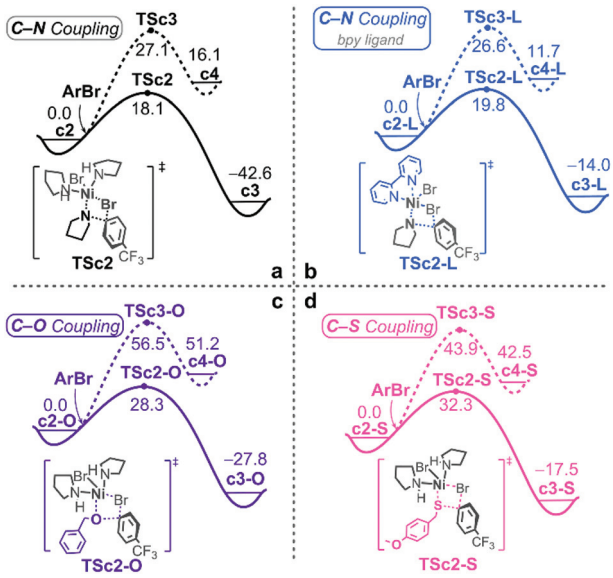

Fig. 7 Gibbs energy profiles ($\Delta G^{\circ}_{298.15}$) of the rate-determining σ-bond metathesis (solid line) and oxidative addition (dashed line) in the radical mechanism using different ligands and substrates. (a) Pyrrolidine as the ligand and one of the substrates (consistent with Fig. 2). (b) bpy as the ligand and pyrrolidine as one of the substrates. (c) Pyrrolidine as the ligand and benzyl alcohol as one of the substrates. (d) Pyrrolidine as the ligand and 4-methoxybenzyl thiol as one of the substrates.

Conclusions

The mechanistic details of the photoredox-mediated Ir^{III}/Ni^{II} dual-catalysed aryl amination have been theoretically disclosed. A radical mechanism merging Ir^{III}–*Ir^{III}–Ir^{II}–Ir^{III} reductive quenching and Ni^{II}–Ni^{III}–Ni^{II}–Ni^{II} catalytic cycles has been proposed (Scheme 3). The reaction starts with a thermodynamically and kinetically favourable single electron transfer process, where photoexcited *Ir(III) is reductively quenched by DABCO to generate the ground-state Ir(II) and DABCO$^{\bullet+}$. The free radical cation reacts with pyrrolidine to successively generate the nitrogen-centred radical coupling partner through hydrogen atom transfer. Then, the nucleophilic radical is captured by the Ni(II) dibromide complex to afford a nickel(III) amino intermediate. The high-oxidation-state Ni(III) can oxidise Ir(II) through the second exergonic single electron transfer providing the Ni(II) amino complex and regenerating photocatalyst Ir(III). Finally, the rate-determining σ-bond metathesis occurs with an energy barrier of 18.1 kcal mol^{-1} to deliver the desired aniline product and regenerate the transition metal catalyst Ni(II) instead of the high-energy stepwise mechanism involving a Ni(IV) intermediate. Interestingly, the electronic processes of σ-bond metathesis exhibit the characteristics of an annular charge transfer ($3d_{Ni} \rightarrow 2p_{RN} \rightarrow \pi_{Ar} \rightarrow 4p_{Br}$). The buried volume calculations and the activation strain analyses indicate that α-substitution on the amine substrate could increase steric hindrance and distortion energy to suppress the σ-bond metathesis, and then may decrease the reac-

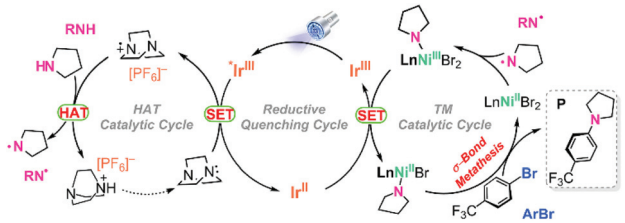

Scheme 3 Full catalytic cycles of photoredox-mediated Ir^{III}/Ni^{II} dual-catalysed aryl amination.

tion yield. Furthermore, the σ-bond metathesis involving Ni(II) is applicable for the C–N cross-coupling rather than C–O and C–S cross-couplings. These perspectives might stimulate new strategies for metallaphotoredox-catalysed cross-coupling reactions in experiments.

Conflicts of interest

There are no conflicts to declare.

Acknowledgements

This work was financially supported by the NSFC (No. 21773025 and 61775212) and the State Key Laboratory of Applied Optics. We acknowledge the National Supercomputing Centre in Shenzhen for providing the computational resources.

Notes and references

1 (*a*) C. C. C. Johansson Seechurn, M. O. Kitching, T. J. Colacot and V. Snieckus, Palladium-Catalyzed Cross-Coupling: A Historical Contextual Perspective to the 2010 Nobel Prize, *Angew. Chem., Int. Ed.*, 2012, **51**, 5062; (*b*) R. Jana, T. P. Pathak and M. S. Sigman, Advances in Transition Metal (Pd, Ni, Fe)-Catalyzed Cross-Coupling Reactions using Alkyl-Organometallics as Reaction Partners, *Chem. Rev.*, 2011, **111**, 1417; (*c*) G. Qiu, Y. Li and J. Wu, Recent Developments for the Photoinduced Ar–X Bond Dissociation Reaction, *Org. Chem. Front.*, 2016, **3**, 1011; (*d*) P. J. Borpatra, B. Deka, M. L. Deb and P. K. Baruah, Recent Advances in Intramolecular C–O/C–N/C–S Bond Formation via C–H Functionalization, *Org. Chem. Front.*, 2019, **6**, 3445.

2 (*a*) P. Ruiz-Castillo and S. L. Buchwald, Applications of Palladium-Catalyzed C-N Cross-Coupling Reactions, *Chem. Rev.*, 2016, **116**, 12564; (*b*) J. Bariwal and E. Van der Eycken, C-N Bond Forming Cross-Coupling Reactions: An Overview, *Chem. Soc. Rev.*, 2013, **42**, 9283.

3 (*a*) T. Maejima, Y. Shimoda, K. Nozaki, S. Mori, Y. Sawama, Y. Monguchi and H. Sajiki, One-Pot Aromatic Amination Based on Carbon–Nitrogen Coupling Reaction Between Aryl Halides and Azido Compounds, *Tetrahedron*, 2012, **68**, 1712; (*b*) A. B. Sheremetev, N. V. Palysaeva, M. I. Struchkova, K. Y. Suponitsky and M. Y. Antipin, Copper-Catalyzed C–N Coupling Reactions of Nitrogen-Rich Compounds-Reaction of Iodofurazans with s-Tetrazinylamines, *Eur. J. Org. Chem.*, 2012, 2266; (*c*) R. Berrino, S. Cacchi, G. Fabrizi and A. Goggiamani, 4-Aryl-2-Quinolones From 3,3-Diarylacrylamides Through Intramolecular Copper-Catalyzed C–H Functionalization/C–N bond Formation, *J. Org. Chem.*, 2012, **77**, 2537.

4 (*a*) S. Zhang, Y. Wang, X. Feng and M. Bao, Palladium-Catalyzed Amination of Chloromethylnaphthalene and Chloromethylanthracene Derivatives With Various Amines, *J. Am. Chem. Soc.*, 2012, **134**, 5492; (*b*) R. M. Stolley, W. Guo and J. Louie, Palladium-Catalyzed Arylation of Cyanamides, *Org. Lett.*, 2012, **14**, 322.

5 (*a*) A. Savateev, I. Ghosh, B. Konig and M. Antonietti, Photoredox Catalytic Organic Transformations using Heterogeneous Carbon Nitrides, *Angew. Chem., Int. Ed.*, 2018, **57**, 15936; (*b*) C. K. Prier, D. A. Rankic and D. W. MacMillan, Visible Light Photoredox Catalysis with Transition Metal Complexes: Applications in Organic Synthesis, *Chem. Rev.*, 2013, **113**, 5322; (*c*) L. Marzo, S. K. Pagire, O. Reiser and B. König, Visible-Light Photocatalysis: Does It Make a Difference in Organic Synthesis?, *Angew. Chem., Int. Ed.*, 2018, **57**, 10034; (*d*) S. Ye, T. Xiang, X. Li and J. Wu, Metal-Catalyzed Radical-Type Transformation of Unactivated Alkyl Halides with C–C Bond Formation Under Photoinduced Conditions, *Org. Chem. Front.*, 2019, **6**, 2183.

6 (*a*) Z. Zuo and D. W. MacMillan, Decarboxylative Arylation of Alpha-Amino Acids via Photoredox Catalysis: A One-Step Conversion of Biomass to Drug Pharmacophore, *J. Am. Chem. Soc.*, 2014, **136**, 5257; (*b*) J. L. Jeffrey, J. A. Terrett and D. W. C. Macmillan, O-H Hydrogen Bonding Promotes H-Atom Transfer from C-H Bonds for C-Alkylation of Alcohols, *Science*, 2015, **349**, 1532; (*c*) J. F. Hartwig, Carbon-Heteroatom Bond Formation Catalysed by Organometallic Complexes, *Nature*, 2008, **455**, 314; (*d*) L. Wang, P. Cheng, X. Wang, W. Wang, J. Zeng, Y. Liang and O. Reiser, Visible-Light Promoted Sulfonamidation of Enol Acetates to A-Amino Ketones Based on Redox-Neutral Photocatalysis, *Org. Chem. Front.*, 2019, **6**, 3771; (*e*) Y. Xu, Z.-J. Xu, Z.-P. Liu and H. Lou, Visible-Light-Mediated De-Aminative Alkylation of N-Arylamines with Alkyl Katritzky Salts, *Org. Chem. Front.*, 2019, **6**, 3902.

7 (*a*) D. P. Hari, P. Schroll and B. Konig, Metal-free, Visible-Light-Mediated Direct C-H Arylation of Heteroarenes with Aryl Diazonium Salts, *J. Am. Chem. Soc.*, 2012, **134**, 2958; (*b*) Q. Y. Meng, J. J. Zhong, Q. Liu, X. W. Gao, H. H. Zhang, T. Lei, Z. J. Li, K. Feng, B. Chen, C. H. Tung and L. Z. Wu, A Cascade Cross-Coupling Hydrogen Evolution Reaction by Visible Light Catalysis, *J. Am. Chem. Soc.*, 2013, **135**, 19052; (*c*) F.-D. Lu, D. Liu, L. Zhu, L.-Q. Lu, Q. Yang, Q.-Q. Zhou, Y. Wei, Y. Lan and W.-J. Xiao, Asymmetric Propargylic Radical Cyanation Enabled by Dual Organophotoredox and Copper Catalysis, *J. Am. Chem. Soc.*, 2019, **141**, 6167.

8 (*a*) J. Twilton, C. Le, P. Zhang, M. H. Shaw, R. W. Evans and D. W. C. MacMillan, The Merger of Transition Metal and Photocatalysis, *Nat. Rev. Chem.*, 2017, **1**, 1; (*b*) J. C. Tellis, D. N. Primer and G. A. Molander, Single-Electron Transmetalation in Organoboron Cross-Coupling by Photoredox/Nickel Dual Catalysis, *Science*, 2014, **345**, 433; (*c*) K. L. Skubi, T. R. Blum and T. P. Yoon, Dual Catalysis Strategies in Photochemical Synthesis, *Chem. Rev.*, 2016, **116**, 10035.

9 (*a*) M. H. Shaw, V. W. Shurtleff, J. A. Terrett, J. D. Cuthbertson and D. W. C. MacMillan, Native

Functionality in Triple Catalytic Cross-Coupling: sp^3 C-H Bonds as Latent Nucleophiles, *Science*, 2016, **352**, 1304; (*b*) Z. Zuo, D. T. Ahneman, L. Chu, J. A. Terrett, A. G. Doyle and D. W. MacMillan, Merging Photoredox with Nickel Catalysis: Coupling of A-Carboxyl sp^3-Carbons with Aryl Halides, *Science*, 2014, **345**, 437.

10 J. A. Terrett, J. D. Cuthbertson, V. W. Shurtleff and D. W. C. MacMillan, Switching on Elusive Organometallic Mechanisms with Photoredox Catalysis, *Nature*, 2015, **524**, 330.

11 (*a*) M. S. Oderinde, M. Frenette, D. W. Robbins, B. Aquila and J. W. Johannes, Photoredox Mediated Nickel Catalyzed Cross-Coupling of Thiols with Aryl and Heteroaryl Iodides via Thiyl Radicals, *J. Am. Chem. Soc.*, 2016, **138**, 1760; (*b*) M. S. Oderinde, N. H. Jones, A. Juneau, M. Frenette, B. Aquila, S. Tentarelli, D. W. Robbins and J. W. Johannes, Highly Chemoselective Iridium Photoredox and Nickel Catalysis for the Cross-Coupling of Primary Aryl Amines with Aryl Halides, *Angew. Chem., Int. Ed.*, 2016, **55**, 13219.

12 (*a*) H. Ren, G.-F. Li, B. Zhu, X.-D. Lv, L.-S. Yao, X.-L. Wang, Z.-M. Su and W. Guan, How Does Iridium(III) Photocatalyst Regulate Nickel(II) Catalyst in Metallaphotoredox-Catalyzed C–S Cross-Coupling? Theoretical and Experimental Insights, *ACS Catal.*, 2019, **9**, 3858; (*b*) B. Zhu, L. K. Yan, Y. Geng, H. Ren, W. Guan and Z. M. Su, IrIII/NiII-Metallaphotoredox Catalysis: The Oxidation State Modulation Mechanism versus the Radical Mechanism, *Chem. Commun.*, 2018, **54**, 5968; (*c*) A. de.Aguirre, I. Funes-Ardoiz and F. Maseras, Four Oxidation States in a Single Photoredox Nickel-Based Catalytic Cycle: A Computational Study, *Angew. Chem., Int. Ed.*, 2019, **58**, 3898; (*d*) K. Kolahdouzan, R. Khalaf, J. M. Grandner, Y. Chen, J. A. Terrett and M. P. Huestis, Dual Photoredox/Nickel-Catalyzed Conversion of Aryl Halides to Aryl Aminooxetanes: Computational Evidence for a Substrate-Dependent Switch in Mechanism, *ACS Catal.*, 2020, **10**, 405; (*e*) M. Yuan, Z. Song, S. O. Badir, G. A. Molander and O. Gutierrez, On the Nature of $C(sp^3)$–$C(sp^2)$ Bond Formation in Nickel-Catalyzed Tertiary Radical Cross-Couplings: A Case Study of Ni/Photoredox Catalytic Cross-Coupling of Alkyl Radicals and Aryl Halides, *J. Am. Chem. Soc.*, 2020, **142**, 7225; (*f*) Y. Liu, Y. Yang, R. Zhu and D. Zhang, Computational Clarification of Synergetic Ru^{II}/Cu^{I}-Metallaphotoredox Catalysis in $C(sp^3)$–N Cross-Coupling Reactions of Alkyl Redox-Active Esters with Anilines, *ACS Catal.*, 2020, **10**, 5030.

13 E. B. Corcoran, M. T. Pirnot, S. Lin, S. D. Dreher and D. W. C. Macmillan, Aryl Amination using Ligand-Free Ni(II) Salts and Photoredox Catalysis, *Science*, 2016, **353**, 279.

14 Z.-H. Qi and J. Ma, Dual Role of a Photocatalyst: Generation of Ni(0) Catalyst and Promotion of Catalytic C–N Bond Formation, *ACS Catal.*, 2018, **8**, 1456.

15 Y. Zhao and D. G. Truhlar, The M06 Suite of Density Functionals for Main Group Thermochemistry, Thermochemical Kinetics, Noncovalent Interactions, Excited States, and Transition Elements: Two New Functionals and Systematic Testing of Four M06-Class Functionals and 12 Other, *Theor. Chem. Acc.*, 2008, **120**, 215.

16 (*a*) H. Ren, G.-F. Du, B. Zhu, G.-C. Yang, L.-S. Yao, W. Guan and Z.-M. Su, Theoretical Mechanistic Study of Nickel(0)/Lewis Acid Catalyzed Polyfluoroarylcyanation of Alkynes: Origin of Selectivity for C–CN Bond Activation, *Organometallics*, 2018, **37**, 2594; (*b*) B. Zhu, L. K. Yan, L. S. Yao, H. Ren, R. H. Li, W. Guan and Z. M. Su, Orthogonal Reactivity of Ni(I)/Pd(0) Dual Catalysts for Ullmann C-C Cross-Coupling: Theoretical Insight, *Chem. Commun.*, 2018, **54**, 7959.

17 P. J. Hay and W. R. Wadt, Ab Initio Effective Core Potentials for Molecular Calculations. Potentials for K to Au Including the Outermost Core Orbitals, *J. Chem. Phys.*, 1985, **82**, 299.

18 K. Fukui, Formulation of the Reaction Coordinate, *J. Phys. Chem.*, 1970, **74**, 4161.

19 M. Mammen, E. I. Shakhnovich, J. M. Deutch and G. M. Whitesides, Estimating the Entropic Cost of Self-Assembly of Multiparticle Hydrogen-Bonded Aggregates Based on the Cyanuric Acid·Melamine Lattice, *J. Org. Chem.*, 1998, **63**, 3821.

20 A. V. Marenich, C. J. Cramer and D. G. Truhlar, Universal Solvation Model Based on Solute Electron Density and on a Continuum Model of the Solvent Defined by the Bulk Dielectric Constant and Atomic Surface Tensions, *J. Phys. Chem. B*, 2009, **113**, 6378.

21 M. Dolg, U. Wedig, H. Stoll and H. Preuss, Energy-Adjusted Abinitio Pseudopotentials for the First Row Transition Elements, *J. Chem. Phys.*, 1987, **86**, 866.

22 M. J. Frisch, H. B. Schlegel, G. E. Scuseria, M. A. Robb, J. R. Cheeseman, G. Scalmani, V. Barone, B. Mennucci, G. A. Petersson, H. Nakatsuji, M. Caricato, X. Li, H. P. Hratchian, A. F. Izmaylov, J. Bloino, G. Zheng, J. L. Sonnenberg, M. Hada, M. Ehara, K. Toyota, R. Fukuda, J. Hasegawa, M. Ishida, T. Nakajima, Y. Honda, O. Kitao, H. Nakai, T. Vreven, J. A. Montgomery Jr., J. E. Peralta, F. Ogliaro, M. Bearpark, J. J. Heyd, E. Brothers, K. N. Kudin, V. N. Staroverov, R. Kobayashi, J. Normand, K. Raghavachari, A. Rendell, J. C. Burant, S. S. Iyengar, J. Tomasi, M. Cossi, N. Rega, J. M. Millam, M. Klene, J. E. Knox, J. B. Cross, V. Bakken, C. Adamo, J. Jaramillo, R. Gomperts, R. E. Stratmann, O. Yazyev, A. J. Austin, R. Cammi, C. Pomelli, J. W. Ochterski, R. L. Martin, K. Morokuma, V. G. Zakrzewski, G. A. Voth, P. Salvador, J. J. Dannenberg, S. Dapprich, A. D. Daniels, O. Farkas, J. B. Foresman, J. V. Ortiz, J. Cioslowski and D. J. Fox, *Gaussian 09 Revision D.01*, Gaussian Inc., Wallingford CT, 2013.

23 C. Y. Legault, *CYLview, 1.0b*, Université de Sherbrooke, 2009 (http://www.cylview.org).

24 (*a*) R. A. Marcus, Electron Transfer Reactions in Chemistry: Theory and Experiment (Nobel Lecture), *Angew. Chem., Int. Ed. Engl.*, 1993, **32**, 1111; (*b*) Y. Li, T. Pullerits, M. Zhao and M. Sun, Theoretical Characterization of the PC60BM:

PDDTT Model for an Organic Solar Cell, *J. Phys. Chem. C*, 2011, **115**, 21865; (*c*) R. A. Marcus, On the Theory of Oxidation-Reduction Reactions Involving Electron Transfer. III. Applications to Data on the Rates of Organic Redox Reactions, *J. Chem. Phys.*, 1957, **26**, 872.

25 T. Lu, *molclus program, Version 1.8.1*, 2019, http://www.keinsci.com/research/molclus.html.

26 A. K. Rappe, C. J. Casewit, K. S. Colwell, W. A. Goddard and W. M. Skiff, UFF, A Full Periodic Table Force Field for Molecular Mechanics and Molecular Dynamics Simulations, *J. Am. Chem. Soc.*, 1992, **114**, 10024.

27 J. L. Jeffrey, F. R. Petronijević and D. W. C. MacMillan, Selective Radical-Radical Cross-Couplings: Design of a Formal β-Mannich Reaction, *J. Am. Chem. Soc.*, 2015, **137**, 8404.

28 F. Wang, L. Zhu, Y. Zhou, X. Bao and H. F. Schaefer 3rd, Is Pd(II)-Promoted Sigma-Bond Metathesis Mechanism Operative for the Pd-PEPPSI Complex-Catalyzed Amination of Chlorobenzene with Aniline? Experiment and Theory, *Chem. – Eur. J.*, 2015, **21**, 4153.

29 (*a*) L. Falivene, R. Credendino, A. Poater, A. Petta, L. Serra, R. Oliva, V. Scarano and L. Cavallo, SambVca 2. A Web Tool for Analyzing Catalytic Pockets with Topographic Steric Maps, *Organometallics*, 2016, **35**, 2286; (*b*) Y. Gao, M. D. Christianson, Y. Wang, J. Chen, S. Marshall, J. Klosin, T. L. Lohr and T. J. Marks, Unexpected Precatalyst σ-Ligand Effects in Phenoxyimine Zr-Catalyzed Ethylene/1-Octene Copolymerizations, *J. Am. Chem. Soc.*, 2019, **141**, 7822.

30 (*a*) F. M. Bickelhaupt and K. N. Houk, Analyzing Reaction Rates with the Distortion/Interaction-Activation Strain Model, *Angew. Chem., Int. Ed.*, 2017, **56**, 10070; (*b*) D. H. Ess and K. N. Houk, Distortion/Interaction Energy Control of 1,3-Dipolar Cycloaddition Reactivity, *J. Am. Chem. Soc.*, 2007, **129**, 10646.

